Analysis of the Thermomechanical Stresses in Double-Wall Effusion Cooled Systems

Elsiddig Elmukashfi[1]
Department of Engineering Science,
University of Oxford,
Park Road,
OX1 3PJ Oxford, UK
e-mail: elsiddig.elmuashfi@eng.ox.ac.uk

Alexander V. Murray
Department of Engineering Science,
University of Oxford,
Park Road,
OX1 3PJ Oxford, UK
e-mail: alexander.murray@eng.ox.ac.uk

Peter T. Ireland
Department of Engineering Science,
University of Oxford,
Park Road,
OX1 3PJ Oxford, UK
e-mail: peter.ireland@eng.ox.ac.uk

Alan C. F. Cocks
Department of Engineering Science,
University of Oxford,
Park Road,
OX1 3PJ Oxford, UK
e-mail: alan.cocks@eng.ox.ac.uk

In this study, thermal stresses in a double-wall cooling system are analyzed. We consider an infinite flat double-wall geometry and assume that it can be represented by an axisymmetric unit cell, wherein the thermal loadings and deformation at the boundaries are determined by periodicity conditions. A thermal model is initially developed to obtain the thermal fields using a combination of empirical correlations and computational fluid dynamics (CFD) analysis. The thermal fields are then analyzed such that both the first-order and higher order approximations are determined. A theoretical solution is derived assuming that the temperature gradient takes place only across the outer skin using the first-order approximations. The solution yields an equibiaxial stress state in the skins, which are driven by the thermal curvature of the outer skin. To investigate other geometrical features and higher order approximations, a finite element model is used to solve Fourier's law of heat conduction and mechanical equilibrium equations. The numerical and theoretical results are found to be in excellent agreement. We determine that the increase of distance between pedestals reduces the stresses. Furthermore, the stress concentration factor at the fillet increases with the increase of both the radius and pedestal diameter and the decrease of the skin thickness. Increasing the number of film holes limits stresses to the external surface of the outer skin. The increase of the Reynolds number in the impingement hole increases the Biot number in the outer skin, which increases the stresses. The higher order approximations of the heat transfer coefficients play a minor role. [DOI: 10.1115/1.4046268]

Keywords: double-wall cooling, thermal stresses, CFD analysis, perturbation analysis, computational fluid dynamics (CFD), heat transfer and film cooling, turbomachinery blading design

1 Introduction

The efficiency of gas turbines continues to be a key incentive in gas turbine research and development. Through elevating turbine thermal efficiency and specific power output, the mainstream core fluid operating temperature is also increased. In turbine environments, these temperatures already exceed the point where mechanical performance is significantly degraded for the nickel superalloys from which the blades are typically constructed. Consequently, these components require active cooling. Advancements in cooling technology are therefore necessary to deal with the further elevation in core temperatures. Such advancements are typically characterized by a reduction in the required coolant volume, and an elevation in the convective efficiency η_{conv} and overall cooling effectiveness ε_0 are achieved, which are given by

$$\eta_{conv} = \frac{T_{c,e} - T_{c,in}}{T_{m,ave} - T_{c,in}} \quad \text{and} \quad \varepsilon_0 = \frac{T_\infty - T_{m,ave}}{T_\infty - T_{c,in}} \tag{1}$$

where $T_{c,e}$ is the coolant temperature at the film hole exit, $T_{c,in}$ is the coolant temperature at the inlet, $T_{m,ave}$ is the average temperature of the metal, and T_∞ is the mainstream temperature. Double-wall, effusion cooling presents one possible advancement in the cooling of turbine blades. Due to the high manufactured porosity of the system, it can be considered to be a quasi-transpiration type cooling technology. The system, as considered here, is characterized by two walls that are mechanically connected via a bank of pedestals, which act to increase the wetted area available for cooling (relative to a conventional multi-pass system) and also act to increase turbulent flow mixing. Coolant enters the blade through impingement holes positioned on the internal wall. The resulting high velocity jet of coolant flow impinges on the hotter outer wall providing a large increase in local convective heat transfer. Film holes are positioned in a closely packed, regular array (characteristic of effusion cooling), on the outer wall; the result of these holes is the creation of a protective film of colder fluid over the outside surface of the blade. A blade incorporating double-wall effusion cooling is shown in Fig. 1.

Research into quasi-transpiration, double-wall type cooling systems has been ongoing since the 1970s. Their lack of widespread implementation has, in-part, resulted from lack of manufacturing

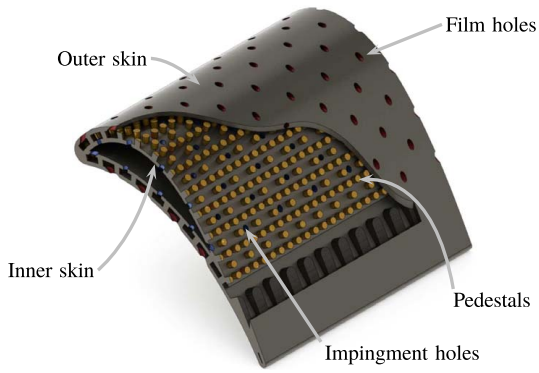

Fig. 1 Double-wall cooled turbine blade concept

[1]Corresponding author.

Contributed by the Heat Transfer Division of ASME for publication in the JOURNAL OF TURBOMACHINERY. Manuscript received July 30, 2019; final manuscript received January 14, 2020; published online February 6, 2020. Assoc. Editor: Giovanna Barigozzi.

capability and cost, particularly during earlier research into the technology. However, what has proven the most significant challenge in their implementation is the thermomechanical stresses that result in the solid under thermal load due to the large temperature gradients between the two walls [1].

In this paper, theoretical and numerical analyses of thermal stresses in a double-wall cooling system are presented. The objective is to understand the nature of different stresses due to the large thermal gradient between hot and cold surfaces and to investigate the role of the different geometrical features and heat transfer fields. We consider the flat-plate double-wall geometry studied by Murray et al. [2]. The geometry is assumed to be built from a basic repeating block, i.e., unit cell, such that all cells are subjected to similar thermal loading, i.e., the temperature and heat transfer coefficients fields. In this study, the unit cell is idealized assuming axisymmetric conditions. Consequently, the distributions of the temperature and heat transfer coefficients are taken to be axisymmetric. The mechanical boundary conditions are defined by the periodicity of the unit cell. To obtain the thermal fields, we developed a thermal model using empirical correlations from the literature and the results obtained by Murray et al. [2]. The thermal fields are then analyzed- and first-order and higher order approximations are obtained. The stress analysis of the thermomechanical boundary value problem is then performed in two steps: (i) theoretical solutions are initially derived for simplified thermal fields to understand the nature of the stresses and (ii) numerical analysis using finite element (FE) models of the unit cell to study the geometrical features and higher order approximations of the thermal fields. The problem statement is presented in Sec. 2. The thermal analysis of the double-wall cooling system using empirical correlations and computational fluid dynamics (CFD) analysis are described in Sec. 3. The details of the stress analysis are then formulated in Sec. 4. The stress analysis results for the different geometrical features and heat transfer fields are presented and discussed in Sec. 5.

2 The Problem Statement

In this work, we focus on studying thermal stresses in a double-wall cooling system due to the large thermal gradient between hot and cold surfaces. We consider the flat-plate double-wall geometry studied by Murray et al. [2]. The geometry is built from a basic repeating block, i.e., unit cell, which contains outer and inner skins, impingement holes, film holes, and pedestals, see Fig. 2. The pedestals are of a circular pin-fin geometry. The height and diameter of the pedestals are denoted by H and D_{pd}, respectively; the spacing between two adjacent pedestals is denoted by L; the impingement hole diameter is denoted by D_i; the film hole diameter is denoted by D_f; and the outer and inner skin thicknesses are taken to be equal and denoted by t. Furthermore, a pedestal makes two fillets with the outer and inner skins that are assumed to be of equal radius R. The values of these dimensions can be found in Sec. 4.4. The thermal analysis of such a system can be performed using different methods, e.g., full CFD analysis of the cooling air and the mainstream [3,4], a decoupled conjugate approach (using CFD for the internal cooling and empirical correlation to model the mainstream) [2], or using suitable empirical correlations [5,6]. The outcome of the thermal analysis, using these methods, is the temperature and heat transfer coefficients on the external surface of the outer skin and the internal walls for a given Reynolds number at the impingement holes and mainstream temperature and velocity. Hence, using the knowledge of the temperature and heat transfer coefficients and suitable mechanical boundary conditions, a thermomechanical boundary value problem can be set up, wherein Fourier's law of heat conduction and mechanical equilibrium equations can be solved to obtain the temperature distribution and stress field in the material.

The main goal of this study is to understand the nature of the stress field and the role of the different geometrical features and internal and external heat transfer factors. We adopt an approach in which the geometry and heat transfer fields are idealized to obtain a theoretical solution of the stress field. More specifically, an axisymmetric idealization of the cooling system and suitable thermal and mechanical boundary conditions are assumed, and the details are presented in Sec. 4. Thereafter, appropriate computational models are developed to investigate the complex features of the problem. The basis of this procedure is presented in the following Secs. 2.1–2.3, and the details are provided in Secs. 3 and 4.

2.1 The Geometrical Idealization. The double-wall cooling system is composed of an infinite array of unit cells. An idealized geometry of this system is shown in Fig. 3(*a*) where the impingement and film holes are omitted. The unit cell is taken to be the simpler geometry in Fig. 3(*b*) such that circular sections of the outer and inner skins are connected by a central pedestal. In this analysis, the thermal fields are assumed to be independent of the θ-direction, and the deformation at the boundary of the unit cell is determined by periodicity conditions. Therefore, axisymmetric conditions are assumed to prevail, and henceforth, an axisymmetric representation of the unit cell will be considered.

2.2 The Temperature and Heat Transfer Coefficient Fields. From the thermal analysis, the temperature profile on the external surface of the outer skin and the heat transfer coefficient and temperature of the coolant on the inner walls (the inner surfaces of the inner and outer skins and the surface of the pedestal) can be obtained for a given impingement jet Reynolds number Re_i, coolant temperature far from the walls (i.e., the temperature at the inlet) T_c, mainstream temperature T_∞, and velocity v_∞. Generally speaking, the distribution of these fields depend on the spatial position, i.e., $\mathbf{r} = \mathbf{r}(r, \theta, z)$. However, assuming axisymmetric conditions, the

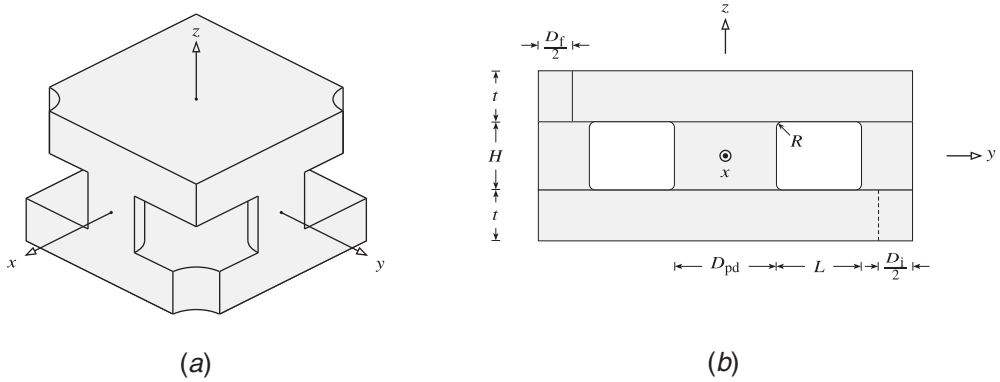

(*a*) (*b*)

Fig. 2 Schematic of the basic building unit of the double-wall cooling system studied by Murray et al. [2]: (*a*) the whole geometry and (*b*) the side view

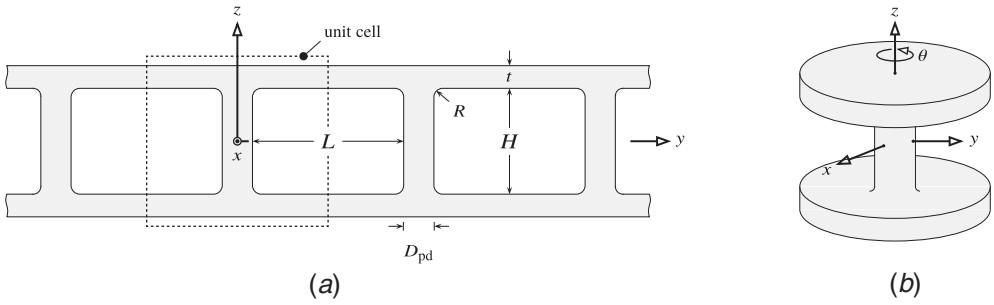

Fig. 3 Schematic of the idealized double-wall cooling system: (*a*) the cross section of the whole geometry and (*b*) the three-dimensional unit cell

surface temperature and heat transfer coefficient can be expressed as follows:

$$T_k = T_k(r, z) \quad \text{and} \quad h_k = h_k(r, z) \tag{2}$$

where T_k is the temperature distribution, h_k is the heat transfer coefficient, with k indicating the surface, i.e., f ≡ external surface of the outer skin (the film), out ≡ internal surface of the outer skin, int ≡ internal surface of the inner skin, pd ≡ pedestal surface, i ≡ inlet of the impingement holes, and e ≡ exit of the film hole. The details of these fields is given in Sec. 3.

2.3 The Thermomechanical Boundary Value Problem. To analyze the double-wall cooling system, we consider the unit cell in Sec. 2.1 under axisymmetric conditions. The temperature and heat transfer coefficient fields are assumed according to Eq. (2), and the mechanical boundary conditions in the symmetry surface are determined by periodicity conditions. The thermal and mechanical boundary conditions are illustrated in Fig. 4. Hence, the temperature boundary conditions are applied on the external surface of the outer skin according to

$$0 \le r \le \frac{1}{2}\left(L + D_{pd}\right) \quad \text{and} \quad z = \frac{1}{2}H + t\text{: } T = T_f(r) \tag{3}$$

and the coolant (contacting air in the internal walls) is at the temperature $T_{c,in}$. The heat transfer coefficient at the internal walls obtained from the thermal analysis of Sec. 2.2 takes the form:

$$0 \le r \le \frac{1}{2}L \quad \text{and} \quad z = -\left(\frac{1}{2}H + t\right)\text{: } h = h_i = \text{const.} \tag{4}$$

$$\frac{1}{2}D_{pd} \le r \le \frac{1}{2}L \quad \text{and} \quad z = -\frac{1}{2}H\text{: } h = h_{int}(r) \tag{5}$$

$$\frac{1}{2}D_{pd} \le r \le \frac{1}{2}L \quad \text{and} \quad z = \frac{1}{2}H\text{: } h = h_{out}(r) \tag{6}$$

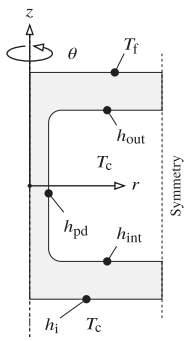

Fig. 4 The thermal and mechanical boundary conditions in the axisymmetric unit cell

$$r = \frac{1}{2}D_{pd} \quad \text{and} \quad -\frac{1}{2}H \le z \le \frac{1}{2}H\text{: } h = h_{pd}(r) \tag{7}$$

The mechanical boundary conditions are defined by the periodicity conditions at the surface of symmetry, i.e., the symmetry line must remain straight, but can rotate and translate. Thus, the periodic boundary conditions are expressed by

$$r = \frac{1}{2}\left(L + D_{pd}\right)\text{: } \varphi = \text{const.} \tag{8}$$

where φ is the angular deflection of the symmetry line perpendicular to the rz-plane, which is determined by the thermal deformations. The resulting thermomechanical boundary value problem can be solved to give the temperature distribution and stress field in the material.

3 The Thermal Model

Literature on the cooling of gas turbines is rife with empirical correlations to predict the Nusselt number for various cooling systems, for example, impingement cooling for various geometries at differing Reynolds numbers and wall spacings or pin-fin/pedestal cooling with different geometrical features and Reynolds number. However, correlations are unavailable (at least in the open literature) for systems such as the double-wall geometry considered here, where the system is an amalgamation of various cooling features that affect the performance of each other. To create a thermal distribution in the two-dimensional section representative of that which would be expected during operation, a thermal model was developed by Murray et al. [7] who utilized a combination of empirical correlations and observations informed by computational simulations. The output of this model is the temperature at the external surface of the outer skin and a Nusselt number (and consequently heat transfer coefficient) distribution over the entire internal surface of the representative geometry. The details of the thermal model are given in Secs. 3.1–3.4.

3.1 The External Surface of the Outer Skin. An empirical correlation is used to determine the film effectiveness, i.e., a modified version of the correlation developed by Goldstein [8]. It yields a better description of the experimental data [7,9], considers span-wise film performance, and accounts for stream-wise development of the films (the effect of multiple film holes). This method replaces the temperature of the freestream for a single film cooling hole with the adiabatic wall temperature that results from the upstream films. Therefore, the temperature at the external surface can be calculated from the adiabatic wall temperature. The film effectiveness achieved via a single hole at a distance x in the stream-wise direction and y in the span-wise direction is expressed by

$$\eta_{f,j} = \frac{M v_\infty D_f}{8\alpha_t\left(x/D_f + x_{decay}\right)} \exp\left[-0.693\left(\frac{y_{1/2}}{y}\right)^2\right] \tag{9}$$

where $\eta_{f,j}$ is the film effectiveness of the jth hole, M is the blowing ratio, D_f is the film hole diameter, α_t is the turbulent thermal diffusivity, x_{decay} is the stream-wise film decay variable, and $y_{1/2}$ is the span-wise distance at which film effectiveness was halved. The stream-wise development of the films is modeled by an additive superposition model that was proposed by Sellers [10] in which a film distribution is obtained for multiple row film ejections. Hence, the overall film effectiveness, η_f, distributions is determined as follows:

$$\eta_f = \prod_{j=1}^{n} \left[1 - \eta_{f,j}(x)\right] \tag{10}$$

It follows that the adiabatic wall temperature T_{aw} can be obtained from the definition

$$\eta_f = \frac{T_\infty - T_{aw}}{T_\infty - T_{c,e}} \tag{11}$$

Figure 5 demonstrates the overall film effectiveness for multiple film holes. It should be mentioned that the distribution of the film temperature yields a sinusoidal function such that the wavelength and amplitude depend on the mainstream characteristics and the size and spacing of the film holes. Hence, in this study, we limit ourselves to the effect of the wavelength and amplitude on the stress field, and further investigations will be presented in future studies.

3.2 The Inner Surface of the Outer Skin. Local heat transfer coefficients can be most significantly affected by impingement cooling [11] where the high velocity coolant jet impacts the hot surface resulting in very high stagnation point heat transfer coefficients, with the flow also acting to increase turbulent mixing after impingement. CFD typically struggles to accurately predict impingement jet heat transfer using lower complexity turbulence models [5], and large eddy simulations, while providing good accuracy, require high computational resources. As a consequence, empirical correlations are typically used in predicting area-averaged or stagnation point Nusselt number based on flow characteristics such as the impingement jet Reynolds number, as well as target plate from impingement hole distance (i.e., H in the given unit cell). In the current model, three correlations were used in predicting impingement zone local Nusselt number. These are as follows:

$121{,}000 \geq \mathrm{Re} \geq 35{,}200$ and $H/D_i = 6$ [12]:

$$\overline{\mathrm{Nu}} = \frac{\mathrm{Re}_i^{0.6}}{3.329 + 0.273\left(x/D_i\right)^{1.3}} \tag{12}$$

$121{,}000 \geq \mathrm{Re} \geq 35{,}200$ and $H/D_i = 12$ [12]:

$$\overline{\mathrm{Nu}} = \frac{\mathrm{Re}_i^{0.6}}{4.577 + 0.436\left(x/D_i\right)^{1.14}} \tag{13}$$

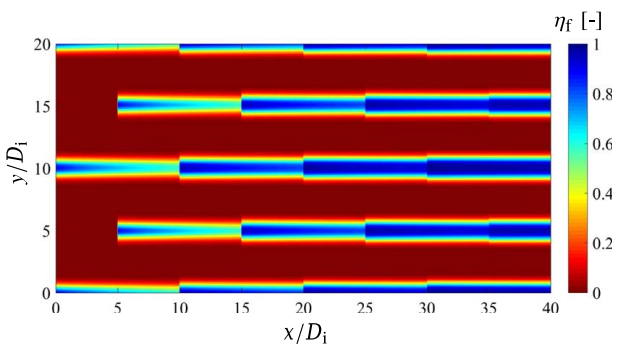

Fig. 5 The distribution of the overall film effectiveness over multiple film ejections in *xy*-plane

$\mathrm{Re} \geq 61{,}000$ and $H/D_i \geq 6$ [13]:

$$\overline{\mathrm{Nu}} = \frac{\left(24 - \left|H/D_i - 7.75\right|\right)\mathrm{Re}_i^{0.76}}{533 + 44\left(x/D_i\right)^{1.295}} \tag{14}$$

where x is the distance on the target surface measured from the stagnation point. It is noted that Eqs. (12)–(14) pertain to the area-averaged Nusselt number based on the radial distance on the target surface. However, of interest here is the variation in local Nusselt number across the target surface. Consequently, the results of the area-averaged $\overline{\mathrm{Nu}}$ at a range of distances from the stagnation point were used to determine the local Nusselt number. Note that Eqs. (12)–(14) each have a range of target plate spacing H and Re over which they are valid. As there are gaps in these ranges, the correlations were used slightly off their calibrated range in some cases. For example, Eq. (12) was used for $9 \geq H/D_i \geq 6$ and Eq. (13) for $12 \geq H/D_i \geq 9$. Outside of the specified ranges of H/D_i and Re, the correlations in Eqs. (12) and (14) were used as the results were deemed to be acceptable for the current application. At very low values of H/D_i (i.e., less than 2), a secondary peak is often observed in the Nusselt number outside of the stagnation point (often displaying higher $\overline{\mathrm{Nu}}$ than at the stagnation point) and are thought to result from heat transfer enhancement from vortex rings in the shear layer [13]. These are disregarded in these correlations; however, the overall effect of this on the overall thermal profile and resulting stress field is deemed to be small. Figure 6 demonstrates the performance of the correlations at varying impingement jet Reynolds numbers and target plate spacing.

3.3 The Impingement and Film Holes. The convective cooling effect within the impingement and film holes was modeled using the Dittus-Boelter correlation, a widely used correlation for predicting average heat transfer within a conduit. The correlation is

$$\overline{\mathrm{Nu}} = 0.023\,\mathrm{Re}_D^{0.8}\,\mathrm{Pr}^n \tag{15}$$

where Pr is the Prandtl number and $n = 0.4$ for fluid that is being heated. While the Dittus-Boelter correlation fails to capture the separation effects attributed with cooling holes of a short distance, as demonstrated in Refs. [14,15], for holes of similar length to diameter ratios to those investigated here, the average heat transfer coefficient around the circumference of the hole is approximately that predicted by the correlation with maximum discrepancies of approximately 35% around the flow separation region. For the current application, the effect of this is small, and so the use of the correlation is deemed acceptable. The results are also compared well to three-dimensional conjugate heat transfer CFD simulations performed in a separate work [2,6].

3.4 The Pedestal. The Nusselt number on all other surfaces was approximated based on conjugate heat transfer CFD simulations that have been performed on double-wall cooling geometries. For these surfaces (the pedestal surfaces and inner skin), high-fidelity CFD simulations were used to predict the surface heat transfer coefficient distributions. The data were then made dimensionless and curves fitted allowing approximate Nusselt number trends to be predicted in geometries not explicitly simulated in CFD. The Nusselt numbers predicted in this way were scaled in differing geometries based on the impingement zone data that were based on empirical correlations. Figure 7 demonstrates one such curve for the distribution in Nusselt number along the length of the pedestal (the side facing the impingement zone). The figure demonstrates the relatively high heat transfer occurring toward the top of the pedestal, a result of the impingement flow striking this section of the pedestal. The trend is very similar to those observed experimentally by Son et al. [16] for protrusions connected to the surface of the impingement target wall. At very large distances

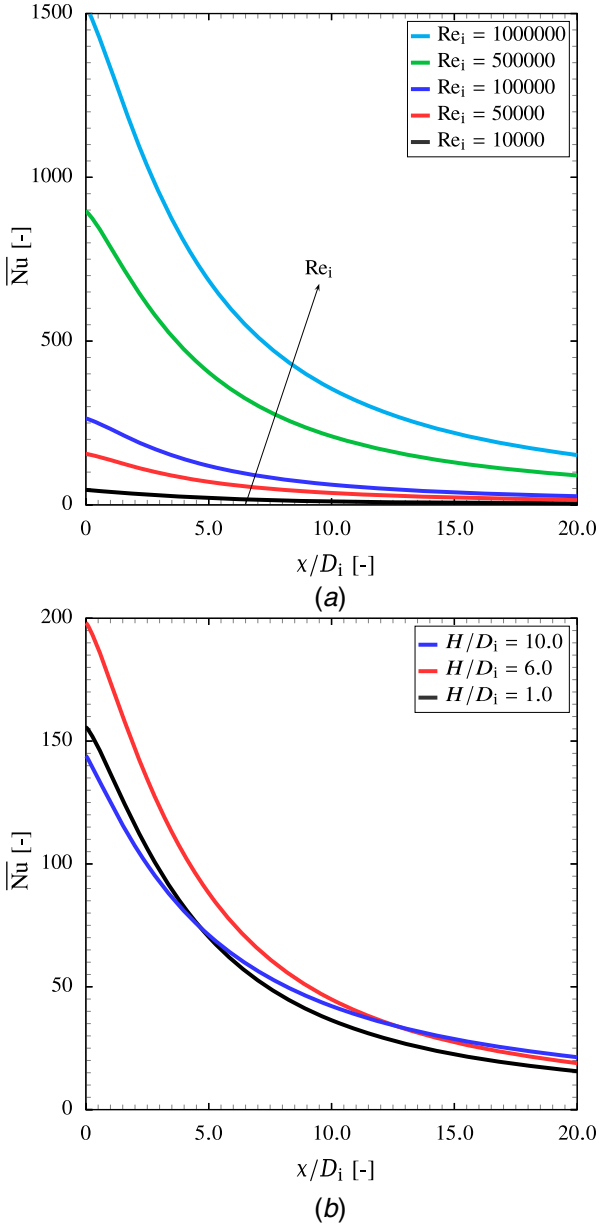

Fig. 6 The variation of Nusselt number $\overline{Nu}$ in local impingement zone at: various Reynolds numbers and $H/D_i = 1.0$ and various target plate spacing and $Re_i = 50{,}000$, i.e., the $\overline{Nu}$ for $H/D_i = 1.0$, 6.0, and 10.0 are determined using Eqs. (14), (12), and (13), respectively

between the impingement zone and the pedestal, this increase in heat transfer was not so prominent; however, at spacings commonly associated with double-wall type cooling geometries, this prediction of Nu distribution is appropriate.

4 Stress Analysis of the Double-Wall Cooling System

In this section, we present the different approaches that are used to analyze the thermomechanical boundary value problem in Sec. 2. We start by analyzing the temperature and the heat transfer coefficient fields as described in Sec. 3 and develop different orders of approximation. A theoretical analysis of the problem is then provided for the first-order approximation. To investigate the influence of the higher order approximations of the temperature and convection coefficient fields, we developed a computational model using the finite element method.

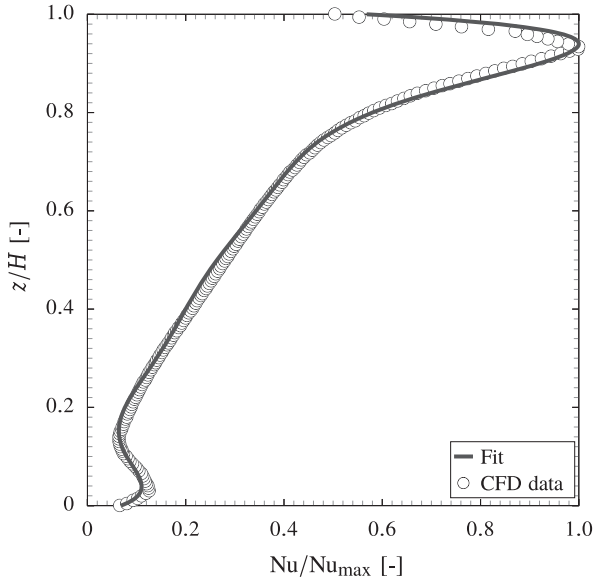

Fig. 7 The variation of Nusselt number Nu along the length of the pedestal (side facing the impingement zone) with fitted curve used in the 2D thermal model. *H* denotes the pedestal height. Note that the target place is located at a *z/H* of unity and the impingement wall at a value of zero.

4.1 The Perturbation Analysis of the Thermal Fields. To study the effect of the complex thermal fields on stress, we have performed a perturbation analysis. In particular, the thermal fields are first examined, and then different orders of approximations are developed. The stress field for each of the approximations is then studied separately. Consequently, for the given linear system, the total stress can be evaluated by superimposing the contributions of the different orders of approximation. Thus, following Taler [17] and considering the thermal boundary conditions in Eqs. (3)–(7), the temperature field in the external surface of the outer skin may be approximated by

$$T_f = \bar{T}_f + \hat{T}_f f_f(\xi_f) \tag{16}$$

where the bar over a symbol ($\bar{\bullet}$) indicates the first-order approximation, the hat over a symbol ($\hat{\bullet}$) indicates the amplitude of the higher order approximations, and f_f are shape functions of the dimensionless local coordinates ξ_f of the external surface of the outer skin. Denote the flux in the internal walls by q_k, which is determined by the htc on the inner walls h_k, where k is the surface. Hence, we assume that the flux q_k is associated with the first-order approximation $\bar{T}_f$ and zero flux with the higher order approximations, i.e., $\hat{T}_f f_f(\xi_f)$. It follows that the stress σ_{ij} at a material point can be determined by

$$\sigma_{ij}(r, z) = \bar{\sigma}_{ij}(r, z) + \hat{\sigma}_{ij}(r, z) \tag{17}$$

where $\bar{\sigma}_{ij}$ and $\hat{\sigma}_{ij}$ are the stress fields that stem from the first-order and higher order approximations, respectively. Furthermore, the temperature T at a material point can be determined in a similar way, i.e., $T(r, z) = \bar{T}(r, z) + \hat{T}(r, z)$.

The film temperature distribution in Eqs. (9)–(11) yields a shape function of the following form

$$f_f = \sin(2\pi\xi_f + \phi_f) \tag{18}$$

where the dimensionless local coordinate for the film is $\xi_f = r/\lambda_f$, λ_f is the wavelength, and ϕ_f is the phase angle. The number of film holes between adjacent pedestals is determined by the wavelength, i.e., the number of film holes within the unit cell is $N_f = (L + D_{pd})/\lambda_f$, and their distribution is obtained by both the

wavelength and the phase angle. For example, a single film hole will be located at the middle distance between the pedestals, i.e., $r = 0.5(L + D_{pd})$, if the wavelength is $\lambda_f = 1.0$ and the phase angle is $\phi = \pi/2$. In this case, the minimum and maximum temperature occur at $r = 0.5(L + D_{pd})$ and $r = 0$, respectively. It should be noted that this case is the best approximation of the unit cell in Fig. 2. The mean and the amplitude of the temperature distribution are determined by the different factors in Eqs. (9)–(11); however, we will not address these dependencies in detail and a qualitative analysis will be performed. Hence, the film temperature distribution can be characterized by the first-order and higher order approximation differences $\Delta\bar{T} = \bar{T}_f - T_c$ and $\Delta\hat{T} = \hat{T}_f - T_c$, respectively, and the film hole wavelength λ_f.

4.2 The Analysis of the Heat Transfer Coefficient. To investigate the htc on the inner walls, the heat transfer coefficient is approximated using a similar expression to Eq. (16):

$$h_k = \bar{h}_k + \hat{h}_k g_k(\xi_k) \tag{19}$$

where g_k are shape functions. The full field h_k and the first-order approximation $\bar{h}_k$ can be used in Sec. 4.1 to determine the flux in the inner walls q_k. Hence, a quantitative analysis of the htc can be performed by prescribing the total field and the first-order approximation in the inner walls separately and compare the stress field $\bar{\sigma}_{ij}(r, z)$. Strictly speaking, the htc approximation in Eq. (19) cannot be used in the perturbation analysis and the flux can be only superimposed [17].

The amplitudes of first-order and higher order terms depend on the Reynolds number at the impingement hole Re_i and the different dimensions of the unit cell, i.e., D_i/t and H/t. Consider the expressions in Eqs. (12)–(15) and the fitting results in Fig. 7, the first-order approximation for the case of impingement hole diameter of $D_i/t = 0.5$, $t = 1$ mm, and $H/t \in [3, 10]$ and different values of Reynolds number are determined and illustrated in Fig. 8. The amplitudes of the higher order approximations are found, using the thermal model in Sec. 3, to be linearly related to the first order by $\hat{h}_{out} = 1.14\bar{h}_{out}$, $\hat{h}_{int} = 11.11\bar{h}_{int}$, and $\hat{h}_{pd} = 5.0\bar{h}_{pd}$. The resulting shape functions are shown in Fig. 9. The heat transfer coefficient on the inner walls can be characterized by Biot numbers of the first-order approximation and the total field, i.e., $\overline{Bi}_k = \bar{h}_k t/K$ and $Bi_k = h_k\, t/K$, respectively, where K is the thermal conductivity of the material.

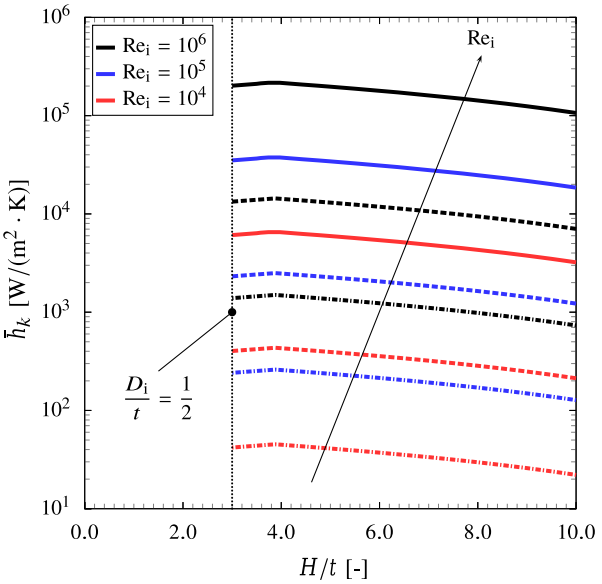

Fig. 8 The first-order term of the heat transfer coefficient $\bar{h}_k$ as a function of the ratio H/t for different values of Reynolds number at the impingement hole Re_i and $D_i/t = 0.5$. The solid lines represent k = out, the dash-dotted lines represent k = int, and dashed lines represent k = pd.

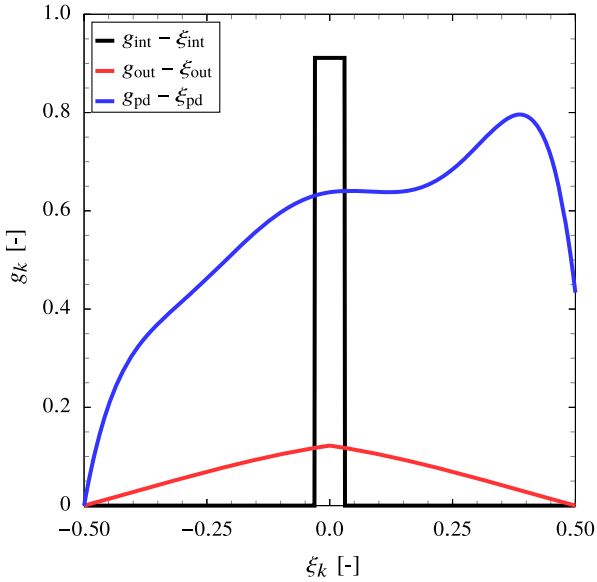

Fig. 9 The shape functions of the heat transfer coefficient for the different surfaces. The dimensionless coordinates ξ_k are defined for the different surfaces as $\xi_{out} = \xi_{int} = [r - 0.5(D_{pd} + L)]/L$ and $\xi_{pd} = z/H$.

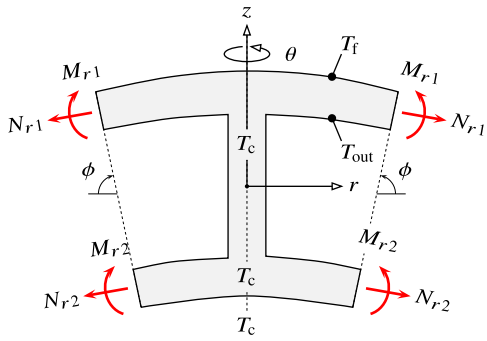

Fig. 10 The internal forces and moments in the idealized axisymmetric unit cell

4.3 Theoretical Analysis. Consider the axisymmetric unit cell in Fig. 4. We assume that the distance between the pedestals is much larger than the thickness of the skins $L \gg t$. Hence, the unit cells can be considered as two circular plates that are connected in the middle by a pedestal. The boundary conditions are defined according to Eqs. (3)–(8). The temperature on the external surface of the outer skin is taken to be the first-order approximation $\bar{T}_f$. The heat transfer coefficient on the inner surface of the outer skin is taken to be the first-order approximation $\bar{h}_{out}$ with Biot number $\overline{Bi}_{out} = \bar{h}_{out} t/K$. The cooling is assumed to be sufficient (i.e., $\overline{Bi}_{out}$ is large enough) such that only the outer skin experiences a thermal gradient. Therefore, the temperature of the other internal surfaces is taken to be equal to the coolant temperature T_c. The moment and force distributions are given by the normal forces per unit depth N_{r1} and N_{r2}, and bending moments per unit length M_{r1} and M_{r2}, in the outer and inner skins, respectively, see Fig. 10. Equilibrium of forces in the r-direction gives

$$N_{r1} + N_{r2} = 0 \tag{20}$$

Taking moments about the center line of the internal skin gives

$$M_{r1} + M_{r2} - N_{r1} \cdot (H + t) = 0 \tag{21}$$

The temperature of the internal surface of the outer skin is determined as follows:

$$T_{\text{out}} = \frac{1}{\overline{\text{Bi}}_{\text{out}} + 1}\left(\bar{T}_{\text{f}} + \overline{\text{Bi}}_{\text{out}} T_{\text{c}}\right) \tag{22}$$

The thermal curvature and strain in the outer skin are, respectively, given by

$$\kappa_{r1}^{\text{T}} = \kappa_{\theta 1}^{\text{T}} = -\frac{\alpha\left(\bar{T}_{\text{f}} - T_{\text{out}}\right)}{t} \quad \text{and} \quad \varepsilon_{r1}^{\text{T}} = \varepsilon_{\theta 1}^{\text{T}} = \frac{1}{2}\alpha\left(\bar{T}_{\text{f}} - T_{\text{out}}\right) \tag{23}$$

where α is the thermal expansion coefficient. Thus, the thermal curvature and strain can be rewritten as follows:

$$\kappa_{r1}^{\text{T}} = \kappa_{\theta 1}^{\text{T}} = -\frac{\overline{\text{Bi}}_{\text{out}}}{\overline{\text{Bi}}_{\text{out}} + 1}\frac{\alpha\Delta\bar{T}}{t} \quad \text{and} \quad \varepsilon_{r1}^{\text{T}} = \varepsilon_{\theta 1}^{\text{T}} = \frac{1}{2}\frac{\overline{\text{Bi}}_{\text{out}}}{\overline{\text{Bi}}_{\text{out}} + 1}\alpha\Delta\bar{T} \tag{24}$$

At larger values of Biot number, the wall temperature of the inner surface of the outer skin approaches the coolant temperature, i.e., when $\overline{\text{Bi}}_{\text{out}} \to \infty$, $T_{\text{out}} = T_{\text{c}}$, and $\overline{\text{Bi}}_{\text{out}}/\left(\overline{\text{Bi}}_{\text{out}} + 1\right) \to 1$, which gives rise to the maximum possible thermal curvature and strain in the outer skin. Furthermore, in order for only the outer skin to experience a thermal gradient, the Biot number should be large enough to prevent the heat from being conducted through the pedestals. Hence, this theoretical analysis will be valid only for the values of Biot number that satisfy this assumption.

Taking the center line of the pedestal as a reference, the rotation of the line of symmetry of the outer skin is as follows:

$$\varphi_1 = \varphi_1^{\text{T}} + \varphi_1^{\text{M}} = \left[-\frac{\overline{\text{Bi}}_{\text{out}}}{\overline{\text{Bi}}_{\text{out}} + 1}\frac{\alpha\Delta\bar{T}}{t} + \frac{M_{r1}}{D(1+\nu)}\right]\left(L + D_{\text{pd}}\right) \tag{25}$$

and that of the inner skin is as follows:

$$\varphi_2 = \varphi_2^{\text{M}} = \frac{M_{r2}}{D(1+\nu)}\left(L + D_{\text{pd}}\right) \tag{26}$$

where φ^{T} and φ^{M} are the thermal and mechanical rotations, $D = E t^3/12(1-\nu^2)$ is the bending stiffness of the skins, E is Young's modulus, and ν is Poisson's ratio. The radial and circumferential strain components in the outer and inner skins are, respectively, given by

$$\varepsilon_{r1} = \varepsilon_{\theta 1} = \frac{1}{2}\frac{\overline{\text{Bi}}_{\text{out}}}{\overline{\text{Bi}}_{\text{out}} + 1}\alpha\Delta\bar{T} + \frac{(1-\nu)N_{r1}}{Et} \tag{27}$$

and

$$\varepsilon_{r2} = \varepsilon_{\theta 2} = \frac{(1-\nu)N_{r2}}{Et} \tag{28}$$

Now, the periodic boundary conditions in Eq. (8) can be rewritten as follows:

$$u_{r2} = u_{r1} + \varphi_1(H + t) \tag{29}$$

$$\varphi_1 = \varphi_2 \tag{30}$$

Solving Eqs. (29) and (30) yields the normal forces as follows:

$$N_{r1} = -N_{r2} = F_N \alpha\Delta\bar{T} E' \tag{31}$$

and the moments as follows:

$$M_{r1} = F_{M_1}\alpha\Delta\bar{T} E' \quad \text{and} \quad M_{r2} = F_{M_2}\alpha\Delta\bar{T} E' \tag{32}$$

where $E' = E/(1-\nu)$, and the functions F_N, F_{M_1}, and F_{M_2} are given by

$$F_N = \left[\frac{(H/t)^2 + (H/t)}{3(H/t)^2 + 6(H/t) + 4}\right]\frac{t}{4\left((H/t)+1\right)}\frac{\overline{\text{Bi}}_{\text{out}}}{\overline{\text{Bi}}_{\text{out}} + 1} \tag{33}$$

$$F_{M_1} = \left[\frac{6(H/t)^2 + 9(H/t) + 4}{3(H/t)^2 + 6(H/t) + 4}\right]\frac{t^2}{24}\frac{\overline{\text{Bi}}_{\text{out}}}{\overline{\text{Bi}}_{\text{out}} + 1} \tag{34}$$

$$F_{M_2} = -\left[\frac{3(H/t) + 4}{3(H/t)^2 + 6(H/t) + 4}\right]\frac{t^2}{24}\frac{\overline{\text{Bi}}_{\text{out}}}{\overline{\text{Bi}}_{\text{out}} + 1} \tag{35}$$

The stress state in the outer skin consists of equibiaxial stresses in the radial and circumferential directions, i.e., $\sigma_r = \sigma_\theta$, which are only functions of z. The maximum value of the nominal stress is at the bottom of the outer skin, $z = H/2$, which can be expressed as follows:

$$\bar{\sigma}_r^{\max} = \bar{\sigma}_\theta^{\max} = \bar{\sigma}_{\max} = \frac{N_{r1}}{t} + \frac{6M_{r1}}{t^2} = \underbrace{\left[\frac{F_N}{t} + \frac{6F_{M_1}}{t^2}\right]}_{F_\sigma}\alpha\Delta\bar{T} E' \tag{36}$$

The multiplier function F_σ depends on the Biot number and the ratio H/t. It increases with increasing the value of $\overline{\text{Bi}}_{\text{out}}$ and H/t, and $\bar{\sigma}_{\max}$ reaches its maximum value when $\overline{\text{Bi}}_{\text{out}} \to \infty$ and $H/t \to \infty$:

$$\bar{\sigma}_{\max} \approx \frac{1}{2}\alpha\Delta\bar{T} E' \tag{37}$$

In this limit, the bending component dominates the expression for the nominal stress in Eq. (36). The minimum value of the nominal stress at the top of the outer skin, $z = H/2 + t$, is then $\bar{\sigma}_{\min} = -\bar{\sigma}_{\max}$. We expect the stress analysis presented above to be valid in the bulk of the outer skin away from the transition with the pedestals. When comparing the results with the detailed finite element calculation presented in Sec. 4.4, we take the nominal stress of Eq. (36) to represent the stress state at $r = 0.5(L + D_{\text{pd}})$. At the fillet at the intersection with the pedestals the maximum principal stress, radial, $\sigma_{1,\max}$, can be expressed as follows:

$$\sigma_{1,\max} = K_r\,\bar{\sigma}_{\max} \tag{38}$$

where K_r is the stress concentration factor in the r-direction, which depends on the fillet radius R, thickness of the outer skin t, and the diameter of the pedestals D_{pd}. It should be noted that the stress concentration factor in the θ-direction, $K_\theta = \sigma_{\theta,\max}/\sigma_\theta$, is generally smaller than K_r, and this will be clarified later in the results in Sec. 5.

4.4 Numerical Analysis. The initial-boundary value problem described in Section 2.3 is numerically solved using the FE code ABAQUS [18]. A coupled thermomechanical analysis is used. The FE analysis requires the solution for an elastic constitutive law and Fourier's law of heat conduction. Suitable material parameters have been used, i.e., for CMSX-4 nickel-base superalloy, in the analysis that are the thermal conductivity coefficient $K = 14$ W/m K, the thermal expansion coefficient $\alpha = 12 \times 10^{-6}$ m/m K, Young's modulus $E = 120$ GPa, and Poisson ratio $\nu = 0.3$ for the temperature range 25 °C–500 °C [19–21]. The values of convection coefficient are used for a specific range of Reynolds numbers as described in Sec. 3. The geometry of the axisymmetric unit cell shown in Fig. 4 is discretized, and a typical finite element mesh is shown in Fig. 11. The initial dimensions are taken as $L = 1$ mm, $H = 1$ mm, $t = 1$ mm, and $D_{\text{pd}} = 1$ mm. A parametric study on different geometrical ratios, i.e., L/t, H/t, and D_{pd}/t, is

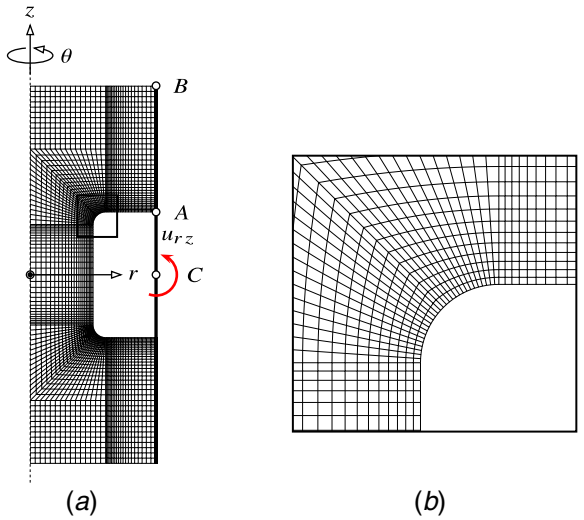

Fig. 11 The finite element mesh of the axisymmetric unit cell: (*a*) the mesh of the whole geometry and (*b*) mesh details around the upper fillet. The periodic boundary conditions are illustrated by the coupling of the degree-of-freedom u_{rz} between the master node *C* and the symmetry surface. Note that points A and B on the outer skin is the location where the maximum and minimum nominal stress $\bar{\sigma}_{max}$ and $\bar{\sigma}_{min}$ are determined, respectively.

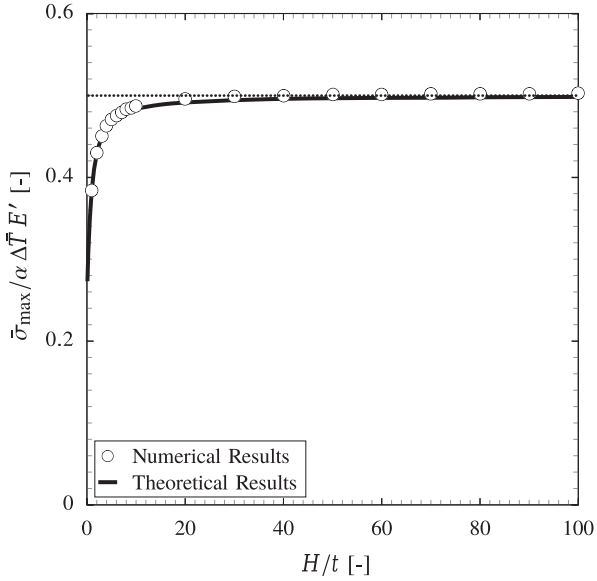

Fig. 12 The comparison between the theoretical and numerical results in terms of the relation between the maximum nominal stress $\bar{\sigma}_{max}/\alpha\Delta\bar{T}E'$ and the geometrical ratio *H*/*t* for the case of $L/t=1$, $D_{pd}/t=1$, $R/t=0.1$, $t=1$ mm, and $\overline{Bi}_{out}=10^3$. The dotted horizontal line depicts the value of the nominal stress in the case of $H/t\to\infty$, i.e., $\bar{\sigma}_{max}/\alpha\Delta\bar{T}E'\approx 0.5$.

performed by keeping t constant and changing other dimensions. The four-node reduced integration bilinear axisymmetric elements (CAX4RT) are used in the discretization. The mesh has 2612 elements, which is found to be sufficient to obtain converged solutions. A uniform refined element region is created adjacent to the fillet to accurately obtain the different stresses, see Fig. 11(*b*). The temperature and heat transfer coefficients are mapped on to the nodes of different surfaces according to Eq. (16). The periodic boundary conditions in Eq. (8) are applied using kinematical coupling. The rotational degree-of-freedom perpendicular to the *rz*-plane, u_{rz}, of the symmetry surface nodes are set to be equal to the master node *C* as illustrated in Fig. 11(*a*).

5 Results and Discussion

5.1 The Effect of the Geometrical Features. Initially, we have studied the relation between the stress and different geometric ratios of the unit cell. In particular, the geometric ratios L/t, H/t, D_{pd}/t, and R/t are considered. The analysis is limited to the case of first-order approximations of the temperature. (The influence of higher order terms is investigated later.) Before evaluating the computational results in detail, it is instructive to compare the theoretical and numerical models. Hence, the computational model is solved for the case of the Biot number $\overline{Bi}_{out}=10^3$ ($Re_i\to\infty$) and different values of the geometrical ratio H/t. The Biot number is chosen to be large enough to keep the pedestal and inner skin temperature equal to the coolant temperature. Figure 12 shows the relation between the maximum nominal stress $\bar{\sigma}_{max}/\alpha\Delta\bar{T}E'$ and the ratio H/t. The figure shows that the theoretical and computational model are in excellent agreement. The result indicates that $\bar{\sigma}_{max}$ increases with the increase of H/t and approaches its maximum value of 0.5 when $H/t\to\infty$. This ratio determines the constraining of the outer skin as in the periodicity condition in Eq. (30).

Figures 13(*a*)–13(*d*) illustrate the stress distributions in the radial, circumferential, and first and third principal directions. The distributions of the radial and circumferential stresses are identical with a larger stress concentration in the case of radial stress at the fillet. The first and third principal stresses are equal to the tensile and compressive radial stresses, respectively. Thus, the results confirm that the stresses are bending stresses, which are generated by the thermal curvature.

The distance between the pedestals, L/t, is now investigated. Figure 14 shows $\bar{\sigma}_{max}/\alpha\Delta\bar{T}E'$ plotted against H/t for $D_{pd}/t=1$, $R/t=0.1$, and different values of L/t. The result implies that the maximum nominal stress decreases with the increase of L/t and approaches the theoretical solution in Eq. (36) for $L/t\geq 2$. Figures 15(*a*)–15(*d*) illustrates the distribution of the nominal stress for different values of L/t, which implies that, in the case of smaller L/t, the nominal stress is influenced by the stress concentration in the fillet. Therefore, the maximum nominal stress becomes dependent on the stress concentration factor of the fillet and the distance L/t. However, the maximum value of the stress in the fillet for the constant values of D_{pd}/t and R/t used in Fig. 15 appears to be constant for the different values of L/t employed (i.e., $\sigma_r^{max}/\alpha\Delta\bar{T}E'\approx 0.68$), which can be explained by the fact that the unit cell is subjected to deformation controlled loading conditions.

We now examine the stress concentration factors K_r and K_θ at the fillet using the FE model for different combinations of the fillet radius R/t and pedestal diameter D_{pd}/t. It should be mentioned that the stress concentration factors are independent of L/t when expressed as a multiple of the maximum nominal stress $\bar{\sigma}_{max}$ determined from the theoretical analysis. Figure 16 shows the stress concentration factors as functions of the dimensionless fillet radius R/t and pedestal diameters D_{pd}/t. The results suggest that the stress concentration factor is larger in the radial direction in comparison with the circumferential direction, and both factors increase with the decrease of R/t and increase of D_{pd}/t.

5.2 Convection Versus Conduction Heat Transfer. In order to study the role of convection cooling on the inner walls, several analyses were performed for the first-order approximation of the heat transfer coefficient and different values of Reynolds number $Re_i=10^4$, 10^5, and 10^6 as in Fig. 8 for $D_i/t=0.5$. For the given values of Re_i, $K=14$ W/m K, $t=1$ mm, and $H/t\in[3,\ 10]$, the Biot number in the inner walls of the outer skin is determined to be $\overline{Bi}_{out}=16$–32, 90–182, and 514–1030, respectively. The Biot number shows a total change of 50% over the given range of Re_i. The temperature at the external surface is taken to be the

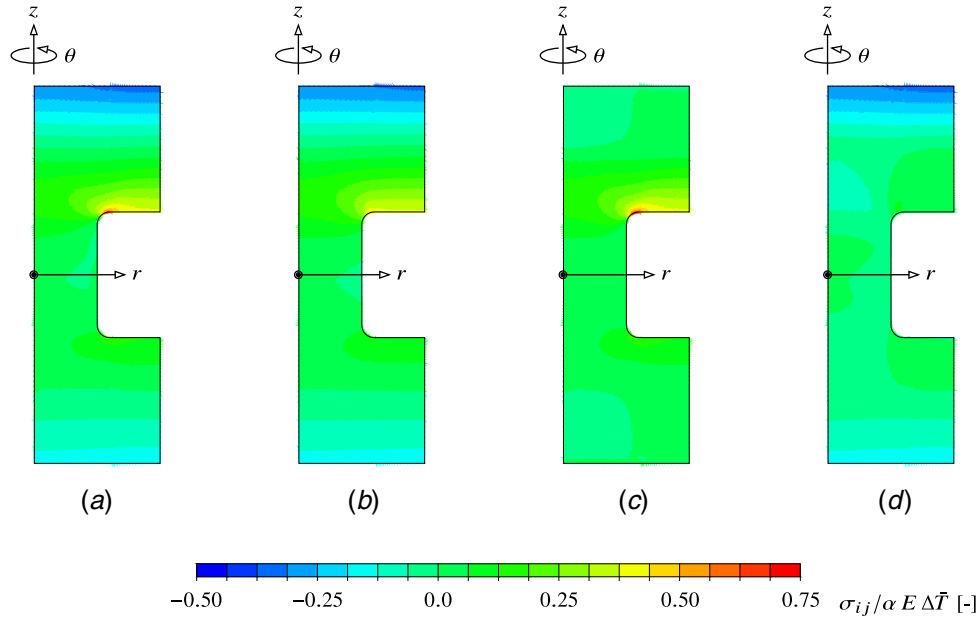

Fig. 13 The distribution of the different stresses for the case of $L/t = 1$, $H/t = 1$, $D_{pd}/t = 1$, $R/t = 0.1$, $t = 1$ mm, and $\overline{Bi}_{out} = 10^3$: (*a*) σ_r, (*b*) σ_θ, (*c*) σ_1, and (*d*) σ_3

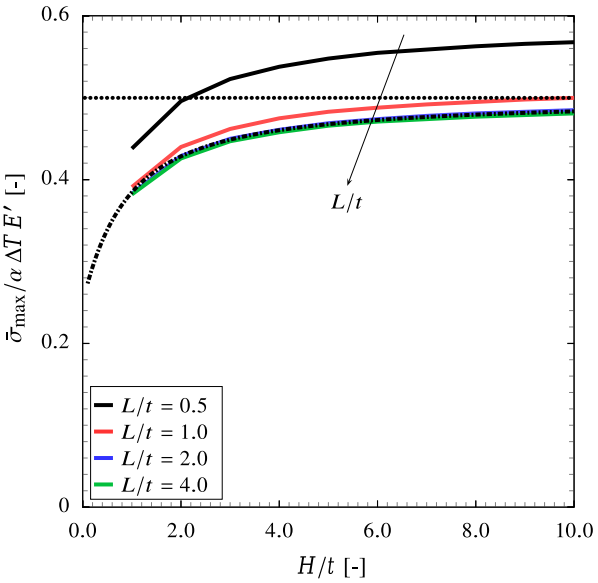

Fig. 14 The relation between the maximum nominal stress $\bar{\sigma}_{max}/\alpha\Delta TE'$ and the geometrical ratio H/t for the case of $H/t = 1$, $D_{pd}/t = 1$, $R/t = 0.1$, $t = 1$ mm, and $\overline{Bi}_{out} = 10^3$ and different values of the ratio L/t. The chained line corresponding to the theoretical solution in Eq. (36). The dotted horizontal line depicts the theoretical value of the nominal stress in the case of $H/t \to \infty$, i.e., $\bar{\sigma}_{max}/\alpha\Delta\bar{T}\,E' \approx 0.5$.

first-order approximation $\bar{T}_f$. Figure 17 shows the relation between $\bar{\sigma}_{max}/\alpha\Delta TE'$ and H/t for different values of the Reynolds number. The result implies that the decrease of the Reynolds number (and consequently the Biot number) results in a significant reduction in the nominal stress for the entire range of H/t. At lower values of the Reynolds number, increasing the ratio H/t yields a further reduction in the stresses. The temperature and nominal stress distributions are plotted in Figs. 18 and 19, respectively, for different values of Reynolds number. The temperature distribution suggests that as the Biot number decreases, the temperature is conducted through the pedestal to the inner skin and its gradient across the outer skin decreases significantly. Hence, the nominal stress reduction is mainly attributed to the reduction in the temperature gradient as suggested by Eq. (36). Increasing the ratio H/t reduces the Biot number, which results in more heat conduction through the pedestals and further reduction in stresses. Moreover, the nominal stress distribution in the outer skin is greater than in the inner skin at higher values of the Biot number, i.e., where the larger temperature gradient is taking place. At lower values of the Biot number, the thermal gradient in the inner skin becomes larger in comparison with the outer skin, which leads to a higher stress in the inner skin. The theoretical solution in Eq. (36) yields similar results.

5.3 The Perturbation Analysis. In this section, we investigate the effect of the higher order approximations of the temperature on the stress field. In particular, as discussed in Sec. 4.1, we examine the second contribution to the stress field in Eq. (17), i.e., $\hat{\sigma}_{ij}$, which stems from the higher order terms in Eq. (16).

The temperature field is taken to be the second term of Eqs. (16) and (18), i.e., $\hat{T}_f f_f$, and the heat flux to the inner wall is taken to be zero. Several analyses were then performed for different values of the wavelength in the range $\lambda_f/L \in [10^{-1}-10^{1}]$ and $H/t \in [3–10]$. To study the nominal stress, we consider two material points A and B that are at $r = 0.5(L + D_{pd})$, $z = 0.5\,H$, and $z = 0.5(H + t)$, respectively, as shown in Fig. 11. Figures 20(*a*) and 20(*b*) illustrate the relation between $\hat{\sigma}_{max}/|\alpha\Delta\hat{T}\,E'|$ and the minimum and maximum values of $\hat{\sigma}_1/|\alpha\Delta\hat{T}\,E'|$, and λ_f/L, respectively, where $\Delta\hat{T} = \hat{T}_f - T_c$. Furthermore, the temperature, nominal, and first principal stress distributions are plotted in Figs. 21–23, respectively, for three values of $\lambda_f/L = 0.1$, 1.0, and 10.0. The results imply that the stresses depend strongly on the wavelength. At lower values of λ_f/L, the nominal stress at point A is compressive (very small), and it is tensile at point B. At intermediate values of λ_f/L, the nominal stress values at points A and B oscillate. In this range, the temperature oscillates along the external surface of the outer skin, which yields a moderate negative temperature gradient across the thickness, leading to higher stresses at the surface and small stresses far from the surface. At higher values of λ_f/L, the nominal stress at points A and B decrease to the zero. The stress reduction is due to the homogeneous temperature distribution along the external surface of the outer skin, which yields a very small temperature gradient across the thickness. The maximum

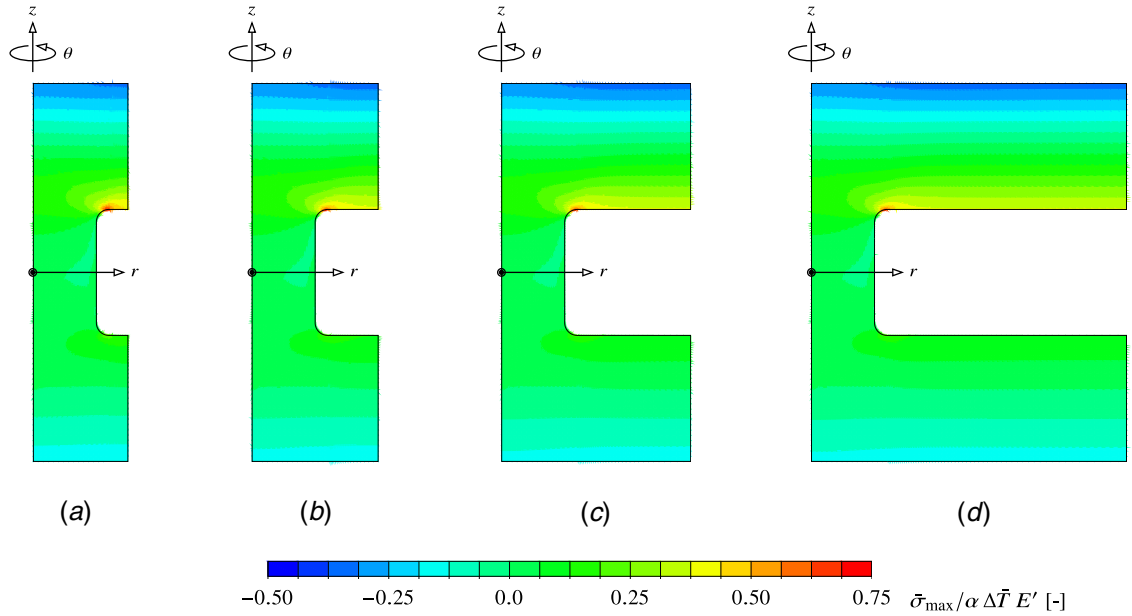

Fig. 15 The distribution of the nominal stress $\bar{\sigma}$ for the case of $H/t = 1$, $D_{pd}/t = 1$, $R/t = 0.1$, $t = 1$ mm, and $\overline{Bi}_{out} = 10^3$ and different values of the ratio L/t: (*a*) 0.5, (*b*) 1.0, (*c*) 2.0, and (*d*) 4.0

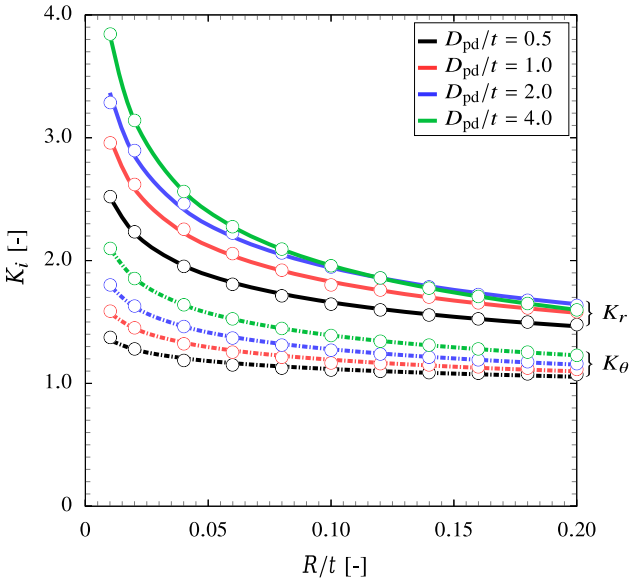

Fig. 16 The stress concentration factors K_r and K_θ as functions of the geometrical ratios R/t and D_{pd}/t for the case of $L/t = 1$, $H/t = 1$, $t = 1$ mm, and $\overline{Bi}_{out} = 10^3$. The solid lines represent K_r, and the dashed lines represent K_θ.

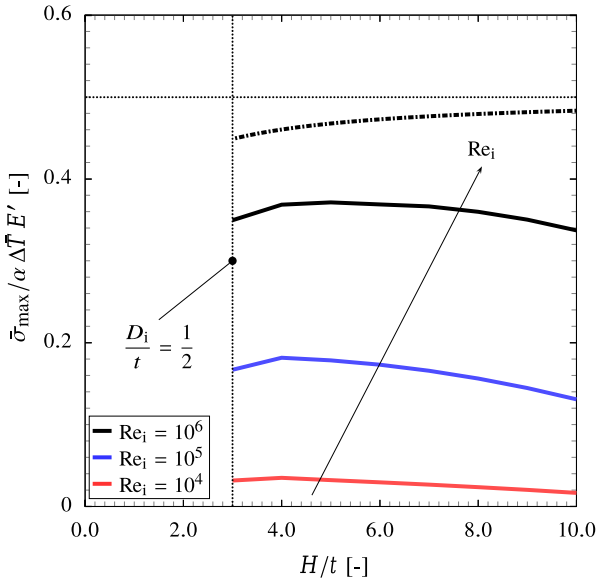

Fig. 17 The effect of convection at the inner walls of the unit cell. The relation between the maximum nominal stress $\bar{\sigma}_{max}/\alpha\Delta\bar{T}E'$ and the geometrical ratio H/t for the case of $L/t = 1$, $D_{pd}/t = 1$, $R/t = 0.1$, $t = 1$ mm, and different values of $\mathrm{Re_i}$. The chained line corresponding to the theoretical solution in Eq. (36). The dotted horizontal line depicts the theoretical value of the nominal stress in the case of $H/t \to \infty$, i.e., $\bar{\sigma}_{max}/\alpha\Delta\bar{T}E' \approx 0.5$.

absolute values of the nominal stress values at points A and B are $\hat{\sigma}_{\max}/\alpha\Delta\hat{T}\,E' \approx 0.001$ and 0.06 at $\lambda_f/L \approx 0.45$ and 0.1, respectively. It should be mentioned that the maximum stress at point A is due to bending deformation and at point B is due to the surface deformation. The maximum and minimum values of the first principal stress are associated with the maximum and minimum nominal stress, see Figs. 22 and 23. Similar oscillatory behavior is observed in the values of the first principal stress. The maximum value of the first principal stress is at the external surface of the outer skin, i.e., $\hat{\sigma}^{(1)}_{1,\max}/\left|\alpha\Delta\hat{T}\,E'\right| \approx 0.72$ at $\lambda_f/L \approx 0.8$, $r = 0$, and $z = 0.5(H + t)$. The minimum value of the first principal stress is $\hat{\sigma}^{(1)}_{1,\min}/\left|\alpha\Delta\hat{T}\,E'\right| \approx -0.03$ in the fillet and at $\lambda_f/L \approx 0.15$. The film hole distribution associated with $\lambda_f/L \approx 10$ gives the minimum stress distribution in the unit cell.

5.4 The Heat Transfer Coefficient Analysis. The higher order approximations of the heat transfer coefficient are now investigated. The total heat transfer coefficient at the inner walls in Eq. (16) and the first-order approximation of the temperature at the external surface of the outer skin $\bar{T}_f$ are used. Similarly, the model is analyzed for the case of $D_i/t = 0.5$, $\mathrm{Re_i} \in [10^2–10^4]$, and $H/t \in [3–10]$, see Figs. 8 and 9. Figure 24 shows the relation

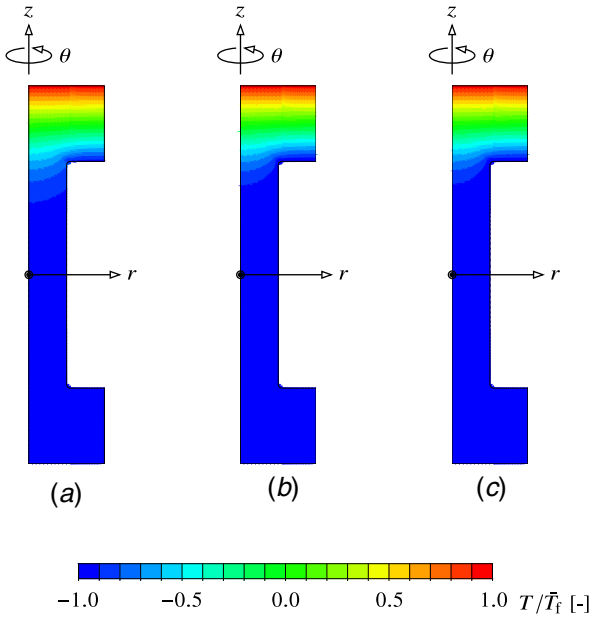

Fig. 18 The distribution of the temperature T for the case of $L/t = 1$, $H/t = 3$, $D_{pd}/t = 1$, $R/t = 0.1$, and $t = 1$ mm and different values of Reynolds number Re_i: (a) 10^4, (b) 10^5, and (c) 10^6

between the nominal stress $\bar{\sigma}_{max}/\alpha\Delta\bar{T}\,E'$ and the ratio H/t for different values of the Reynolds number and heat transfer coefficient (the first-order approximation $\bar{h}_k$ and full field h_k). The result shows that reducing the Reynolds number (and consequently, the Biot number) yields a significant reduction in the nominal stress for the entire range of H/t. Furthermore, the differences between the stress values of the full field and the first-order approximation are significantly small, i.e., $\lesssim$10%, which can be explained by the fact that the higher order approximations' amplitude $\hat{h}_k$ is smaller than the first-order $\bar{h}_k$, i.e., the maximum value of the higher order terms in the inner surface of the outer skin is approximately $0.12\tilde{h}_k$ and that of the first-order term is $0.88\tilde{h}_k$.

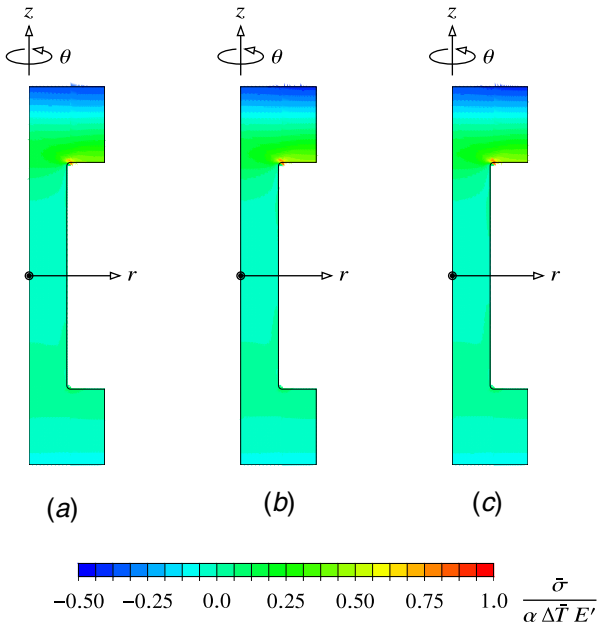

Fig. 19 The distribution of the nominal stress $\bar{\sigma}$ for the case of $L/t = 1$, $H/t = 1$, $D_{pd}/t = 1$, $R/t = 0.1$, and $t = 1$ mm and different values of the Reynolds number Re_i: (a) 10^4, (b) 10^5, and (c) 10^6

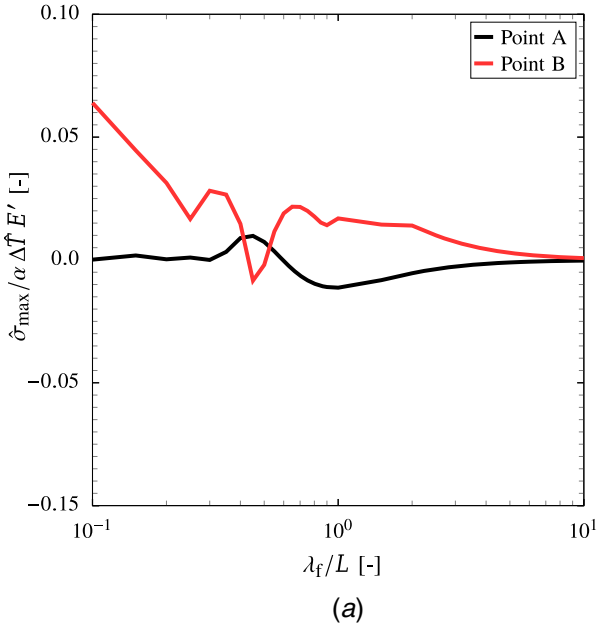

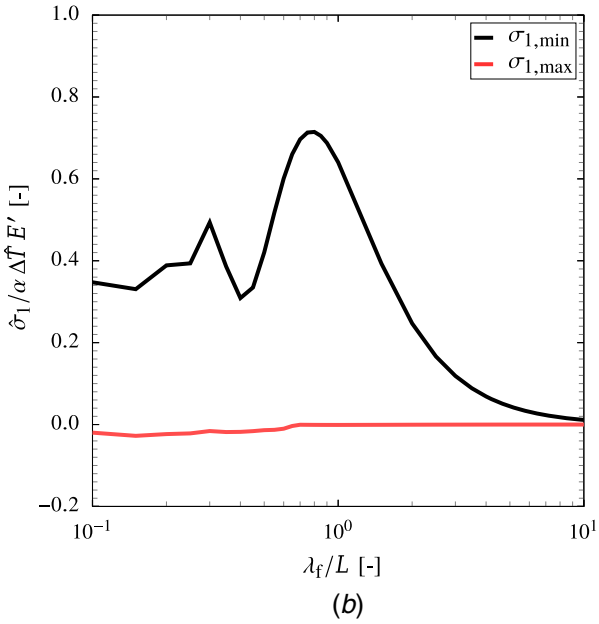

Fig. 20 The relation between the stress $\hat{\sigma}_{ij}/|\alpha\Delta\hat{T}\,E'|$ and the wavelength λ_f/L for the case of $L/t = 1$, $H/t = 1$, $D_{pd}/t = 1$, $R/t = 0.1$, and $t = 1$ mm: (a) the nominal stress and (b) the first principal stress

6 Concluding Remarks

In this paper, we have investigated thermal stresses in an infinite flat double-wall cooling system. We have considered an idealized axisymmetric unit cell in which the thermal boundary conditions have been applied in terms of the film temperature on the external surface of the outer skin and the heat transfer coefficients at the inner walls. The mechanical boundary conditions are implemented using periodicity conditions. The thermal fields are obtained using empirical correlations and CFD analysis for a given velocity and temperature of the mainstream, Reynolds number at the impingement hole and coolant temperature. Theoretical solutions are initially developed using first-order approximations of the thermal fields and assuming that the thermal conductivity is limited to the outer skin (i.e., it is valid for larger values of Biot number $\overline{Bi}_{out}$). A computational model is then developed to solve Fourier's law

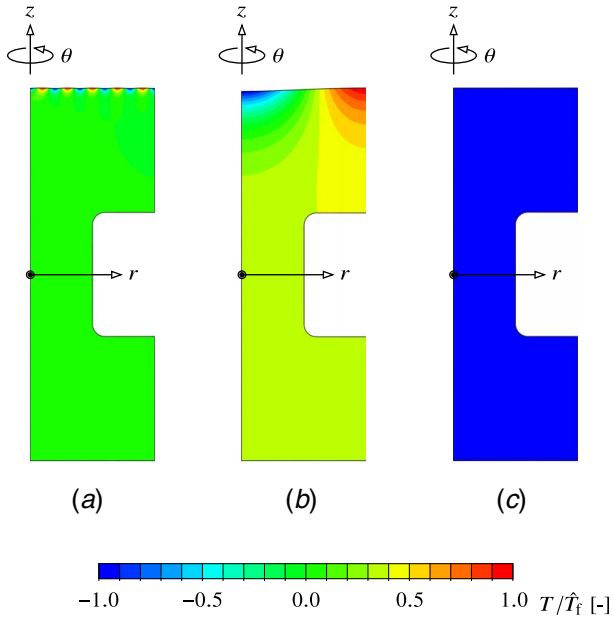

Fig. 21 The distribution of the temperature T for the case of $L/t = 1$, $H/t = 1$, $D_{pd}/t = 1$, $R/t = 0.1$, and $t = 1$ mm and different values of the Reynolds number wavelength λ_f: (a) $\lambda_f = 0.1$, (b) $\lambda_f = 1$, and (c) $\lambda_f = 10$

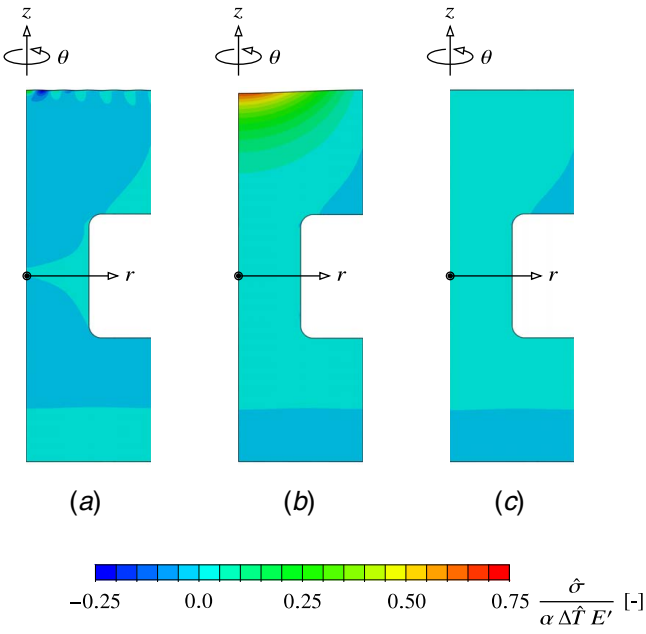

Fig. 22 The distribution of the nominal stress $\hat{\sigma}$ for the case of $L/t = 1$, $H/t = 1$, $D_{pd}/t = 1$, $R/t = 0.1$, and $t = 1$ mm and different values of wavelength λ_f: (a) $\lambda_f = 0.1$, (b) $\lambda_f = 1$, and (c) $\lambda_f = 10$

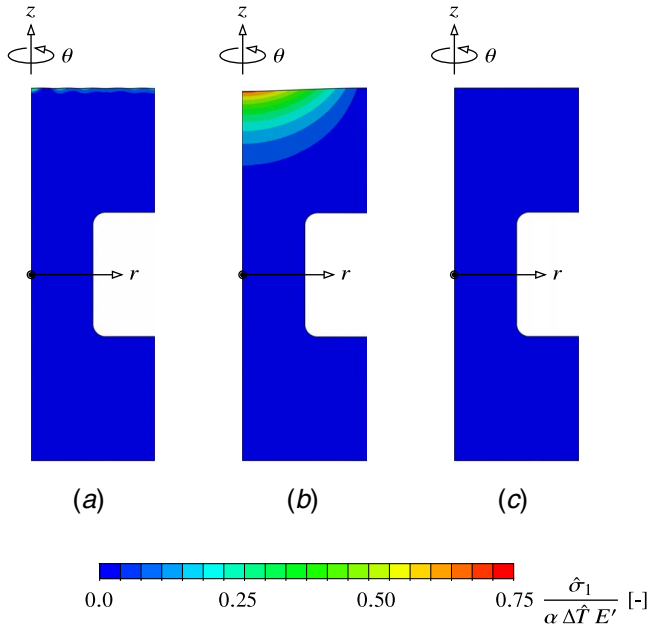

Fig. 23 The distribution of the principal stress $\hat{\sigma}_1$ for the case of $L/t = 1$, $H/t = 1$, $D_{pd}/t = 1$, $R/t = 0.1$, and $t = 1$ mm and different values of the wavelength λ_f: (a) $\lambda_f = 0.1$, (b) $\lambda_f = 1$, and (c) $\lambda_f = 10$

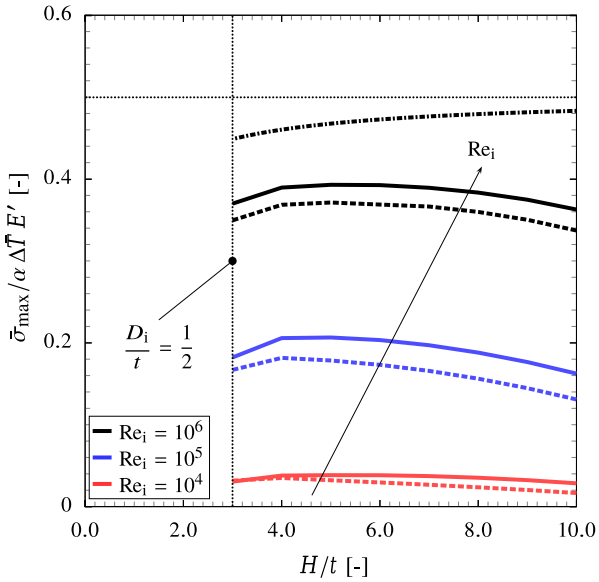

Fig. 24 The relation between the nominal stress $\bar{\sigma}_{max}/\alpha \Delta \bar{T} E'$ and the ratio H/t for the case of $L/t = 1$, $D_{pd}/t = 1$, $R/t = 0.1$, $t = 1$ mm, and different values of Re_i. The full and dashed lines corresponding to the full field and first-order approximations of the htc, respectively. The chained line corresponding to the theoretical solution in Eq. (36). The dotted horizontal line depicts the theoretical value of the nominal stress in the case of $H/t \to \infty$, i.e., $\bar{\sigma}_{max}/\alpha \Delta \bar{T} E' \approx 0.5$.

of heat conduction and mechanical equilibrium equations using the commercial finite element code ABAQUS. This model is then used to study different geometrical features and higher order approximations of the thermal fields. The main findings are summarized as follows:

(1) At high values of the Reynolds number at the impingement hole, i.e., $Re_i \geq 10^5$, the thermal curvature due to the thermal gradient in the outer skin causes the stresses in the skins. At lower Reynolds number, heat is conducted through the pedestal to the inner skin, which might result in a larger thermal gradient in the inner skin. Therefore, in these case, the thermal curvature in the inner skin drives the deformation.

(2) As a result of first-order approximations of the film temperature, the maximum principal stress occurs at the fillet between the pedestal and outer skin due to stress concentration at higher values of the Reynolds number. At lower Reynolds number, it might change to the fillet between the pedestal and inner skin. The maximum principal stress

occurs at the external surface of the outer skin, i.e., at $r=0$ and $z=0.5(H+t)$, in the case of higher order approximations. Hence, depending on the temperature amplitudes $\Delta\bar{T}_f$, $\Delta\hat{T}_f$, and Reynolds number, the maximum principal stress might change its magnitude and location.

(3) Increasing the pedestals height-skin thickness ratio H/t increases the nominal stress, which approaches a constant value, i.e., $\bar{\sigma}_{max}/\alpha\Delta TE' = 0.5$, as $H/t \to \infty$. The nominal stress decreases with the increase of the distance between pedestals; however, the maximum principal stress remains constant due to the constancy of the thermal curvature. The stress concentration factor at the fillet increases with the increase of the pedestal diameter and decreases with the increase of its radius and skin thickness.

(4) The higher order approximation of the film temperature is characterized by the number and distribution of the film holes and is expressed in terms of the wavelength λ_f and the phase angle ϕ_f. Increasing the number of film holes limits stresses to the external surface of the outer skin. Moderate and smaller numbers result in higher and lower stresses, respectively, as the inhomogeneous temperature distribution at the external surface of the outer skin becomes homogeneous.

(5) The higher order approximation of the heat transfer coefficients plays a minor role due to the fact that their amplitudes are less than 10% of the first-order approximation.

These calculations provide a physical insight into geometric factors that determine how stresses develop in double-wall effusion cooled systems during thermal cycling. This understanding can be used to help identify structural configurations, which provide good mechanical performance. This will be addressed in the subsequent work.

Acknowledgment

The authors are grateful to both Rolls-Royce plc and EPSRC under grant EP/P000878/1 for supporting the research presented in this paper.

Nomenclature

Symbols

h = heat transfer coefficient (W/(m^2 K))
l = length scale (m)
t = the outer and inner skin thicknesses (m)
v = velocity (m/s)
D = the diameter (m)
E = Young's modulus (N/m^2)
H = the height of the pedestals (m)
K = thermal conductivity (W/(m K))
L = the spacing between two adjacent pedestals (m)
M = the moment per unit thickness (N m/m)
N = the normal force per unit thickness (N/m)
R = the radius of the fillets between the pedestals and the outer and inner skins (m)
T = temperature (K)
c_p = specific heat capacity (J/K)
u_i = displacement vector ($i=1, 2, 3$)
Nu = Nusselt number, $\mathrm{Nu}=h\ l/K$
Pr = Prandtl number, $\mathrm{Pr}=c_p\ \mu/K$
Re = Reynolds number, $\mathrm{Re}=\rho v\ l/\mu$
α = the thermal expansion coefficient (K^{-1})
ε_{ij} = engineering strain tensor
κ = the curvature
μ = dynamic viscosity (Pa · s)
ν = Poisson's ratio
ρ = density (kg/m^3)
σ_{ij} = Cauchy stress tensor (Pa)

Superscripts and Subscripts

c = coolant property
f = film property
i = impingement property
m = metal property
o = overall
in = inlet property
int = internal surface of the inner skin property
out = internal surface of the outer skin property
pd = pedestal property
∞ = main stream property

References

[1] Krewinkel, R., 2013, "A Review of Gas Turbine Effusion Cooling Studies," Int. J. Heat Mass Transfer, **66**, pp. 706–722.
[2] Murray, A. V., Ireland, P. T., and Rawlinson, A. J., 2017, "An Integrated Conjugate Computational Approach for Evaluating the Aerothermal and Thermomechanical Performance of Double-Wall Effusion Cooled Systems," ASME Turbo Expo 2017: Turbomachinery Technical Conference and Exposition, Charlotte, NC, June 26–30, p. V05BT22A015.
[3] York, W. D., and Leylek, J. H., 2003, "Three-Dimensional Conjugate Heat Transfer Simulation of an Internally-Cooled Gas Turbine Vane," ASME Turbo Expo 2003, Collocated With the 2003 International Joint Power Generation Conference, pp. 351–360.
[4] Facchini, B., Tarchi, L., Toni, L., and Ceccherini, A., 2010, "Adiabatic and Overall Effectiveness Measurements of an Effusion Cooling Array for Turbine Endwall Application," ASME J. Turbomach., **132**(4), p. 041008.
[5] Zuckerman, N., and Lior, N., 2005, "Impingement Heat Transfer: Correlations and Numerical Modeling," ASME J. Heat Transfer, **127**(5), pp. 544–552.
[6] Ngetich, G. C., Ireland, P. T., Murray, A. V., and Romero, E., 2018, "A 3D Conjugate Approach for Analysing a Double-Walled Effusion-Cooled Turbine Blade," ASME Turbo Expo 2018: Turbomachinery Technical Conference and Exposition, p. V02DT46A017.
[7] Murray, A. V., Ireland, P. T., Wong, T. H., Tang, S. W., and Rawlinson, A. J., 2018, "High Resolution Experimental and Computational Methods for Modelling Multiple Row Effusion Cooling Performance," Int. J. Turbomach. Propul. Power, **3**(1), p. 4.
[8] Goldstein, R. J., 1971, "Film Cooling," Adv. Heat Transfer, **7**, pp. 321–379.
[9] Baldauf, S., Schulz, A., and Wittig, S., 1999, "High Resolution Measurements of Local Effectiveness by Discrete Hole Film Cooling," ASME 1999 International Gas Turbine and Aeroengine Congress and Exhibition, p. V003T01A020.
[10] Sellers, J. P., 1963, "Gaseous Film Cooling With Multiple Injection Stations," AIAA J., **1**(9), pp. 2154–2156.
[11] Han, J.-C., Dutta, S., and Ekkad, S., 2012, *Gas Turbine Heat Transfer and Cooling Technology*, CRC Press, Boca Raton, FL.
[12] Goldstein, R., and Behbahani, A., 1982, "Impingement of a Circular Jet With and Without Cross Flow," Int. J. Heat Mass Transfer, **25**(9), pp. 1377–1382.
[13] Goldstein, R., Behbahani, A., and Heppelmann, K. K., 1986, "Streamwise Distribution of the Recovery Factor and the Local Heat Transfer Coefficient to an Impinging Circular Air Jet," Int. J. Heat Mass Transfer, **29**(8), pp. 1227–1235.
[14] Gillespie, D., Byerley, A., Ireland, P., Wang, Z., Jones, T., and Kohler, S., 1996, "Detailed Measurements of Local Heat Transfer Coefficient in the Entrance to Normal and Inclined Film Cooling Holes," ASME J. Turbomach., **118**(2), pp. 285–290.
[15] Gillespie, D. R., 1998, "Intricate Internal Cooling Systems for Gas Turbine Blading," Ph.D. thesis, University of Oxford, Oxford, UK.
[16] Son, C., Dailey, G., Ireland, P., and Gillespie, D., 2005, "An Investigation of the Application of Roughness Elements to Enhance Heat Transfer in an impingement Cooling System," ASME Turbo Expo 2005: Power for Land, Sea, and Air, pp. 465–479.
[17] Taler, J., 2014, "Superposition Method for Multidimensional Heat Conduction Problems," Encyclopedia Thermal Stresses, pp. 4708–4718.
[18] Abaqus, H., 2016, "User's Manual," Version 6.14, Karlsson and Sorensen, Inc., Providence, RI.
[19] Siebörger, D., Knake, H., and Glatzel, U., 2001, "Temperature Dependence of the Elastic Moduli of the Nickel-Base Superalloy CMSX-4 and Its Isolated Phases," Mater. Sci. Eng. A, **298**(1–2), pp. 26–33.
[20] Quested, P., Brooks, R., Chapman, L., Morrell, R., Youssef, Y., and Mills, K., 2009, "Measurement and Estimation of Thermophysical Properties of Nickel Based Superalloys," Mater. Sci. Technol., **25**(2), pp. 154–162.
[21] Scholz, A., Wang, Y., Linn, S., Berger, C., and Znajda, R., 2009, "Modeling of Mechanical Properties of Alloy CMSX-4," Mater. Sci. Eng. A, **510**, pp. 278–283.